By contrast, the emergent monopoles that we identify here are sources of the emergent magnetic field that follows Dirac's quantization condition for monopoles (*17*); i.e., they carry one quantum of emergent flux. Furthermore, in spin-ice at zero magnetic field, the monopoles are "deconfined"; i.e., it requires only a finite amount of energy to separate monopole and antimonopole. In the skyrmion phase, the situation is different (similar arguments apply to the helical phase): Deep in the skyrmion phase, it requires a finite amount of energy per length to zip two skyrmions together. Consequently, there is a linear potential (i.e., a finite string tension) holding monopole and antimonopole together. Only during the conversion from one phase to the other, the string tension vanishes or becomes negative. In disordered materials, the string tension may be a random function that competes with potentials pinning the monopoles.

An interesting open question is whether phases of deconfined emergent monopoles in chiral magnets exist, where monopoles and antimonopoles proliferate as independent entities. A candidate for such a phase is the metallic state of MnSi at high pressure. Its properties differ markedly from those of conventional metals [the resistivity is proportional to $T^{3/2}$ over almost three decades in $T$ (*23*)], with highly unconventional "partial" magnetic order on intermediate time and length scales (*24*) and an unconventional Hall signature (*15*). Further experiments and theoretical studies are needed to study the connection of the partial order in MnSi with the emergent monopoles and the electronic properties in the non–Fermi liquid phase of MnSi.

### References and Notes

1. P. Chaikin, T. Lubensky, *Principles of Condensed Matter Physics* (Cambridge Univ. Press, Cambridge, 1995).
2. N. Manton, P. Suttcliff, *Topological Solitons* (Cambridge Univ. Press, Cambridge, 2004).
3. S. Mühlbauer *et al.*, *Science* **323**, 915 (2009).
4. W. Münzer *et al.*, *Phys. Rev. B* **81**, 041203(R) (2010).
5. X. Z. Yu *et al.*, *Nature* **465**, 901 (2010).
6. X. Z. Yu *et al.*, *Nat. Mater.* **10**, 106 (2011).
7. S. Seki, X. Z. Yu, S. Ishiwata, Y. Tokura, *Science* **336**, 198 (2012).
8. T. Adams *et al.*, *Phys. Rev. Lett.* **108**, 237204 (2012).
9. X. Yu *et al.*, *Proc. Natl. Acad. Sci. U.S.A.* **109**, 8856 (2012).
10. A. Tonomura *et al.*, *Nano Lett.* **12**, 1673 (2012).
11. F. Jonietz *et al.*, *Science* **330**, 1648 (2010).
12. T. Schulz *et al.*, *Nat. Phys.* **8**, 301 (2012).
13. G. Volovik, *J. Phys. C Solid State Phys.* **20**, L83 (1987).
14. J. Zang, M. Mostovoy, J. H. Han, N. Nagaosa, *Phys. Rev. Lett.* **107**, 136804 (2011).
15. R. Ritz *et al.*, *Nature* **497**, 231 (2013).
16. A. Neubauer *et al.*, *Phys. Rev. Lett.* **102**, 186602 (2009).
17. P. A. M. Dirac, *Proc. R. Soc. Lond., A Contain. Pap. Math. Phys. Character* **133**, 60 (1931).
18. C. Castelnovo, R. Moessner, S. L. Sondhi, *Nature* **451**, 42 (2008).
19. D. J. P. Morris *et al.*, *Science* **326**, 411 (2009).
20. See supplementary materials on *Science* Online.
21. S. Zhang, S. S.-L. Zhang, *Phys. Rev. Lett.* **102**, 086601 (2009).
22. C. Pfleiderer *et al.*, *J. Phys. Condens. Matter* **22**, 164207 (2010).
23. C. Pfleiderer, S. R. Julian, G. G. Lonzarich, *Nature* **414**, 427 (2001).
24. C. Pfleiderer *et al.*, *Nature* **427**, 227 (2004).

**Acknowledgments:** We thank R. Bamler, P. Böni, K. Everschor, L. Fritz, M. Garst, R. Georgii, S. Mayr, and the team of FRM II, and, especially, D. Meier. We are grateful to B. Pedersen for checking the orientation of our sample on the diffractometer HEIDI at FRM II. Financial support through European Research Council AdG 291079 (TOPFIT) and through SFB 608, SFB TR 12, and SFB TR 80 of the Deutsche Forschungsgemeinschaft (DFG) is gratefully acknowledged. A.B. A.C., and J.K. acknowledge support through the TUM Graduate School, S.B. and C.S. through the Bonn-Cologne Graduate School of Physics and Astronomy (BCGS), D.K. through RTG 1401/2 (DFG), J.S. by the Australian Research Council through a Future Fellowship (FT110100523), and S.B. through the Emmy-Noether group (DFG) of L. Fritz.

**Supplementary Materials**
www.sciencemag.org/cgi/content/full/340/6136/1076/DC1
Materials and Methods
Supplementary Text
Figs. S1 to S8
References (*25*–*35*)

31 December 2012; accepted 19 April 2013
10.1126/science.1234657

---

# Measurements of Energetic Particle Radiation in Transit to Mars on the Mars Science Laboratory

C. Zeitlin,[1]* D. M. Hassler,[1] F. A. Cucinotta,[2] B. Ehresmann,[1] R. F. Wimmer-Schweingruber,[3] D. E. Brinza,[4] S. Kang,[4] G. Weigle,[5] S. Böttcher,[3] E. Böhm,[3] S. Burmeister,[3] J. Guo,[2] J. Köhler,[3] C. Martin,[3] A. Posner,[6] S. Rafkin,[1] G. Reitz[7]

**The Mars Science Laboratory spacecraft, containing the Curiosity rover, was launched to Mars on 26 November 2011, and for most of the 253-day, 560-million-kilometer cruise to Mars, the Radiation Assessment Detector made detailed measurements of the energetic particle radiation environment inside the spacecraft. These data provide insights into the radiation hazards that would be associated with a human mission to Mars. We report measurements of the radiation dose, dose equivalent, and linear energy transfer spectra. The dose equivalent for even the shortest round-trip with current propulsion systems and comparable shielding is found to be 0.66 ± 0.12 sievert.**

Understanding the radiation environment inside a spacecraft carrying humans to Mars or other deep space destinations is critical for planning future crewed missions. Without major advances in propulsion systems, a large share of the radiation exposure on such missions will be incurred during outbound and return travel, when the spacecraft and its inhabitants will be exposed to the radiation environment in interplanetary space, shielded only by the spacecraft itself. Here we report measurements of the energetic particle radiation environment inside the Mars Science Laboratory (MSL) during its cruise to Mars between 6 December 2011 and 14 July 2012, with implications for future human Mars missions.

Two forms of radiation pose potential health risks to astronauts in deep space. There is a chronic low-dose exposure to galactic cosmic rays (GCRs), and there is also the possibility of short-term exposures to the solar energetic particles (SEPs) that are sporadically accelerated close to the Sun by solar flares and coronal mass ejections. GCRs tend to be highly energetic, highly penetrating particles that are not stopped by the modest depths of shielding on a typical spacecraft. The distributions of the kinetic energy of GCRs are broad and vary according to the ion species and the phase of the solar cycle, with peaks near 1000 MeV for protons and 500 to 600 MeV per nucleon for heavier ions, with tails extending to much higher energies. The flux of GCRs consists of about 85% protons, which are sparsely ionizing (except at the very end of their ranges), and about 14% helium ions. The remainder of the flux consists of heavier ions referred to as "HZE particles" [high (H) atomic number (Z) and high energy (E)]. HZE particles are densely ionizing, producing biological effects that differ from those produced by sparsely ionizing radiation; there is considerable uncertainty about the effects of HZE particles on biological systems (*1*, *2*).

The SEPs of concern for astronaut safety are typically protons with kinetic energies up to a few hundred mega–electron volts. SEP events can produce very large fluxes of these particles, as well as helium and heavier ions. With the exceptions of extreme and rare SEP events, there is little enhanced flux at the higher energies (above 100 MeV per nucleon) typical of GCRs. The comparatively low energy of typical SEPs means that shielding is much more effective against SEPs than GCRs.

Conventional risk assessment methods (*1*, *3*–*5*) rely on measured distributions of kinetic energy

---

[1]Southwest Research Institute, Boulder, CO, USA. [2]NASA Johnson Space Center, Houston, TX, USA. [3]Christian Albrechts University, Kiel, Germany. [4]Jet Propulsion Laboratory, California Institute of Technology, Pasadena, CA, USA. [5]Southwest Research Institute, San Antonio, TX, USA. [6]NASA Headquarters, Washington, DC, USA. [7]German Aerospace Center (DLR), Cologne, Germany.

*Corresponding author. E-mail: zeitlin@boulder.swri.edu

To appreciate the physics of the merging of the skyrmions observed experimentally and numerically, we note that both the topological nature of the skyrmions and their interaction with electrons are best described (*12*) in terms of the (fictitious) emergent electromagnetic fields (*13*, *14*, *21*)

$$\mathbf{B}_i^e = \frac{\hbar}{2}\varepsilon_{ijk}\hat{n}\cdot(\partial_j\hat{n}\times\partial_k\hat{n}),$$
$$\mathbf{E}_i^e = \hbar\hat{n}\cdot(\partial_i\hat{n}\times\partial_t\hat{n}) \qquad (1)$$

where $\hat{n}(\mathbf{r},t) = \mathbf{M}/|\mathbf{M}|$ is the local orientation of the magnetization, $\partial_i = \partial/\partial r_i$ and $\varepsilon_{ijk}$ is the totally antisymmetric tensor. Taken together $\mathbf{B}_i^e$ and $\mathbf{E}_i^e$ account for the Berry phase that the spin of a conduction electron accumulates when following the magnetic texture adiabatically. The experimental consequences have been detected directly in terms of an additional (topological) contribution to the Hall signal and an emergent electric field, providing evidence of the motion of the skyrmions (*12*, *15*, *16*).

As the integral of $\mathbf{B}^e/\hbar$ over a surface describes the solid angle covered by $\hat{n}$, the emergent magnetic flux of each skyrmion is exactly given by one (negative) flux quantum $\int\mathbf{B}^e d\sigma = -\frac{2\pi\hbar}{|q^e|} = -\Phi_0$ [we use a convention, where the conduction electrons of the majority (minority) bands carry the charge 1/2 (−1/2), respectively (*12*)]. Therefore, the topologically quantized winding number or, equivalently, the quantized magnetic flux has to change when two skyrmions merge. Because of the topological nature of the winding number, this is in fact only possible by a singular field configuration for which the local magnetization vanishes at a point in space. The implications for the topological properties may thereby be seen by integrating $\mathbf{B}^e$ over a closed surface $\partial\Omega$ of the volume $\Omega$

$$\oint_{\partial\Omega}\mathbf{B}^e d\sigma = \int_\Omega \nabla\mathbf{B}^e d\mathbf{r} = -\frac{2\pi}{|q^e|}(N_{\text{out}}^s - N_{\text{in}}^s)$$
$$= \mp\Phi_0 \qquad (2)$$

Here $N_{\text{out}}^s$ ($N_{\text{in}}^s$) is the number of ingoing (outgoing) skyrmion lines, respectively. Hence, when two ingoing skyrmions merge, there must be a singular field configuration, a hedgehog defect with winding number +1, which creates one quantum of emergent magnetic flux. The point of coalescence therefore carries a quantized emergent magnetic charge; i.e., it is an "emergent magnetic monopole." Similarly, when an ingoing single skyrmion line splits into two, an antimonopole with winding number −1 is located at the point of separation. Figure 1B shows schematically such an antimonopole; the location of a monopole (MP) is marked by an arrow in Fig. 3A. Monopoles and antimonopoles are related by a time-reversal symmetry transformation, $\mathbf{M} \to -\mathbf{M}$, followed by a rotation by π around an axis perpendicular to the magnetic field.

The merging of skyrmions at the surface of the crystal observed in our MFM experiment implies that one of two processes has taken place. Either the merging of the skyrmion lines has started in the bulk and the antimonopole, which zipped two skyrmion lines together, has moved through the surface. Or, when the merging of two skyrmion lines started at the surface, a monopole has entered the surface. As the line segments can be interpreted as elongated skyrmions, also the merging of the segments implies that an antimonopole (monopole) has moved out of (into) the surface, respectively.

Both our experiments and our numerical calculations suggest that the merging of skyrmions underlies the conversion of the skyrmion phase into the helical phase. The change of topology is thereby governed by the creation and motion of topological point defects, which we identify as emergent magnetic monopoles and antimonopoles. Figure 3C shows the density of separate (*20*) monopoles and antimonopoles during the field sweep. A comparison of Fig. 3, B and C, shows that the destruction of skyrmions at the surface is directly associated with the proliferation of monopoles and antimonopoles [see also fig. S8]. We expect that the energy and dynamics of the monopoles govern the metastability (*4*, *22*) of the skyrmion phase. Because of their singular core, monopoles are expected to pin much stronger to impurities in the sample, an effect not taken into account in our simulations.

It is instructive to compare the emergent magnetic monopoles discussed here with the magnetic monopoles considered in spin ice (*18*, *19*). Monopoles in spin ice are sources of the "real" magnetic *H*-field, but their magnetic charge is not quantized and depends on microscopic details.

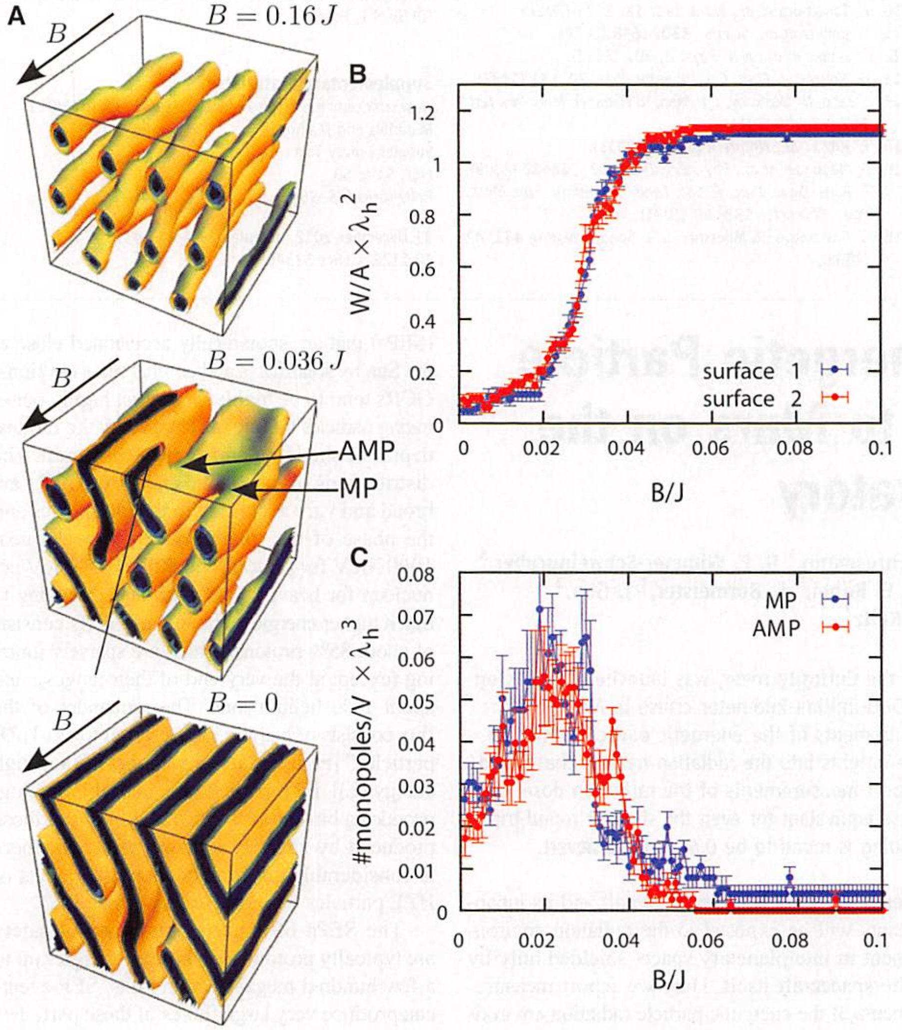

**Fig. 3. Monte Carlo simulation for a system first field cooled at $B = 0.16\,J$ (B‖[110]) down to $T = 0.6\,J$.** [See (*20*) for other temperatures.] After the cool-down, the field is reduced at constant temperature. Below a critical field, skyrmions start to touch and merge. **(A)** Typical magnetic configurations shown by contour surfaces of equal magnetization in [110] direction for $B = 0.16\,J$, $B = 0.036\,J$, and $B = 0$. The arrows labeled MP and AMP point to a monopole and antimonopole, respectively. **(B)** Winding number $W$ (or, equivalently, number of skyrmions) per area in units of the helical wavelength $\lambda_h^2$ on the front and back surface of the simulated box computed while $B$ is reduced. **(C)** Number of monopoles (MP) and antimonopoles (AMP) per volume in units of $\lambda_h^3$. The plots show averages over 15 cooling cycles; error bars denote standard deviations of the mean.

or linear energy transfer (LET) in water (in units of kilo–electron volts per micrometer). These spectra are integrated against the quality factors (*Q*'s) to obtain the dose equivalent (*H*) as defined by the International Commission on Radiological Protection (*6*). The dose equivalent is measured in sieverts (Sv) and has been related to lifetime cancer risk via long-term population studies (*7*). Additional details can be found in the supplementary materials.

The Curiosity rover, with the Radiation Assessment Detector (RAD) mounted to its top deck, was inside the MSL spacecraft on its trip to Mars, sitting immediately beneath the Descent Stage and above the heat shield. Because the spacecraft and internal structures provided shielding against the deep space radiation environment, the RAD measured a mix of primary and secondary particles. (Secondary particles are those produced by nuclear or electromagnetic interactions of primary ions as they traverse the spacecraft mass.) A simplified model of the mass around the RAD was created at the Jet Propulsion Laboratory, working from a highly detailed model of the spacecraft (*8*). Shielding around the instrument was complex, with most of the solid angle lightly shielded (areal density <10 g/cm$^2$) and the remainder broadly distributed over a range of depths up to about 80 g/ cm$^2$. The greatest depths correspond to trajectories through a fuel tank filled with hydrazine. Shielding distributions on the International Space Station are similarly complex (*9*). In contrast, the Apollo spacecraft were lightly shielded, averaging 4.5 g/cm$^2$ of aluminum (*10*). A human crew on a Mars mission would, like the RAD, be exposed to a mixture of primary and secondary radiation, but details of the shielding distribution would probably be quite different. In particular, a spacecraft carrying humans would probably be designed to have a more homogeneous mass distribution, with few if any light-shielded paths into the inhabited areas.

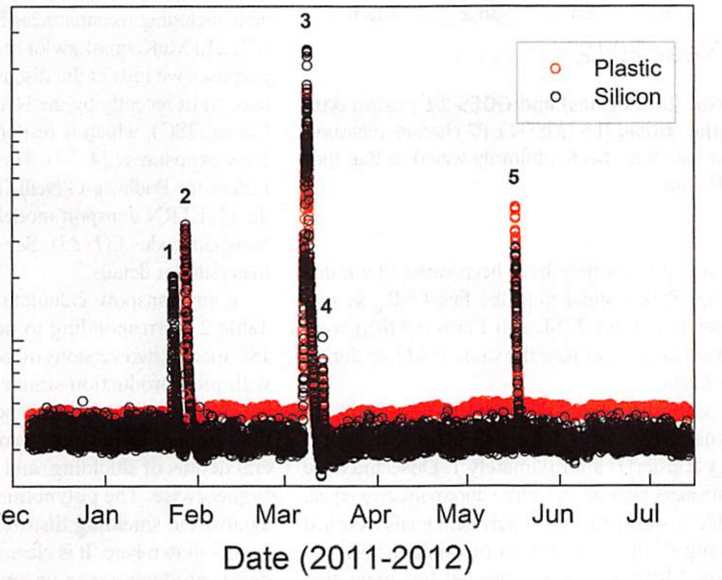

**Fig. 1. Dose rates recorded in a silicon detector (black circles) and in a plastic scintillator (red circles) during the MSL's cruise to Mars.** The observed SEP events are indicated by numerals. The data have been averaged over 15.5-min intervals. Occasional brief gaps can be seen, usually caused by the RAD having been powered off so that other activities could take place on the spacecraft without interference. For a given incident flux, the dose rate in silicon is generally less than the dose rate in plastic because of the comparatively large ionization potential of silicon.

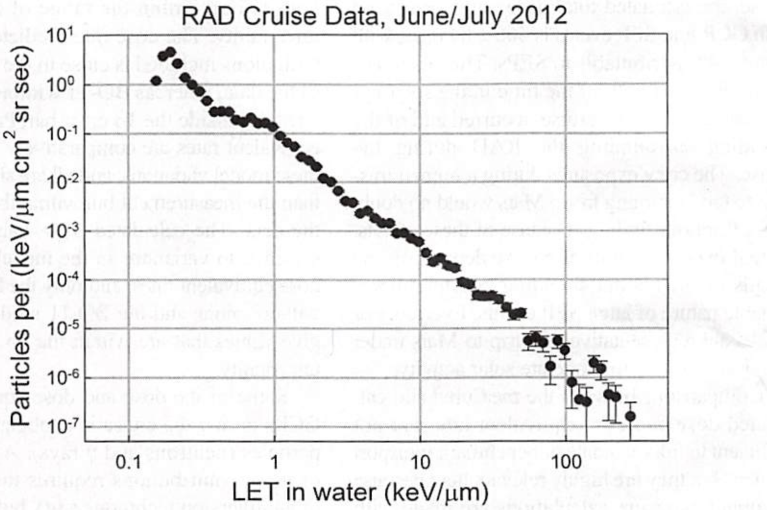

**Fig. 2. The LET spectrum in water measured using charged particle coincidence events.** Energy deposited in silicon has been converted to $\text{LET}_\infty$ in water. Below about 50 keV/μm, the plotting symbols are larger than the error bars.

The RAD instrument has been described in detail in the literature (*11*, *12*). A brief overview is given in the supplementary materials. Two concurrent measurements of dose are made, one using a silicon detector and the other using a plastic scintillator. The latter has a composition similar to that of human tissue, and it is also more sensitive to neutrons than are the silicon detectors. The two dose-rate measurements obtained during the cruise are shown in Fig. 1 (*13*). These measurements differ from previously reported data in that they were obtained in deep space under complex shielding, whereas particle detectors in other deep space missions have measured the unshielded radiation environment.

Measurements were taken from 6 December 2011 to 14 July 2012 (*14*). For solar quiet times, the GCR dose rate in silicon averaged 332 ± 23 μGy/day after subtraction of the background from Curiosity's radioisotope thermoelectric generator (*13*). The error on this result is dominated by uncertainty in the calibration of the silicon detector. To compare with the measured dose rate in plastic and with model predictions, the dose rate in silicon can be converted, approximately, to dose rate in water. A constant factor was applied to relate energy lost per unit of path length (*dE*/*dx*) in silicon to LET in water (*15*). After conversion, the dose rate in water as measured in the silicon detector was found to be 481 ± 80 μGy/day, which is identical within uncertainties to the 461 ± 92 μGy/day measured in the plastic scintillator.

We used data from the final month of the cruise (a time period during which no SEP events were observed) to obtain the charged-particle LET distribution for GCR primary particles and GCR-induced secondary particles. We used the resulting spectrum, after conversion of the deposited energy in silicon to LET in water (Fig. 2), to obtain the average quality factor <*Q*>, which was found to be 3.82 ± 0.25. The uncertainty on <*Q*> is approximately equal parts statistical (low count rate at high LET) and systematic (calibration, conversion from silicon to tissue, and subtraction of the radioisotope thermoelectric generator background radiation). Combining the tissue dose rate measurement with <*Q*> yields a GCR dose equivalent rate of 1.84 ± 0.33 mSv/day. It is important to

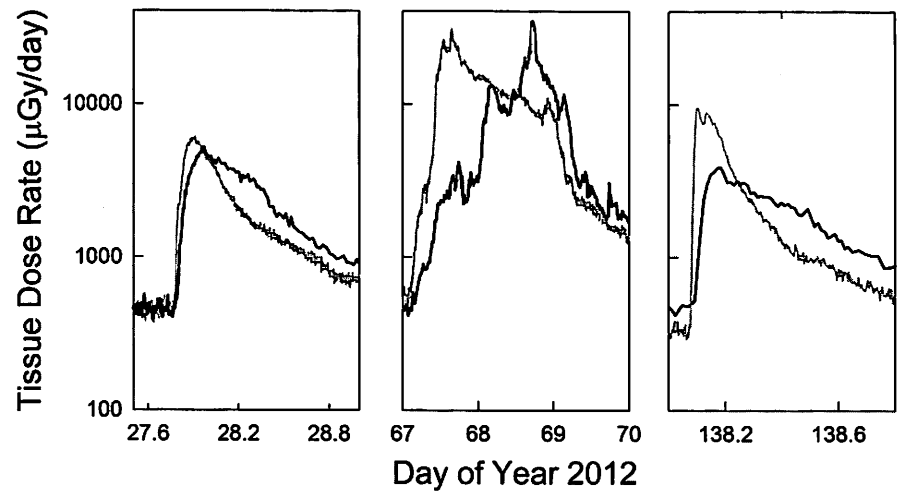

**Fig. 3. RAD dose rates as measured by the B detector (black lines) and GOES-11 proton data (gray lines) for three solar events observed during the cruise.** The GOES-11 P7 channel measures protons in the energy range from 165 to 500 MeV; those data have been arbitrarily scaled so that they have approximately the same quiet-time level as the RAD data.

**Table 1. Dose equivalents measured during SEP events.**

| Time period (2012) | Integrated dose equivalent (mSv) |
|---|---|
| 23 to 29 January | 4.0 |
| 7 to 15 March | 19.5 |
| 17 to 18 May | 1.2 |
| Cruise SEP Total | 24.7 |

note that the measurements depended strongly on heliospheric conditions during the cruise (i.e., near solar maximum), and on the shielding that surrounded the RAD.

Five SEP events were observed during the cruise to Mars: two from 23 to 29 January, two from 7 to 15 March, and one on 17 May (Fig. 2). The events during 7 to 11 March were the largest in terms of dose, but the May event is of interest as well because it was a ground-level event at Earth, and the RAD data indicate that the spectrum was relatively hard. For this event, unlike the other four SEP events, the dose rate recorded in the plastic scintillator exceeded that recorded in the silicon detectors, even though the plastic scintillator is more shielded than the silicon detectors (*16*).

We compare RAD SEP event data to data from the Geostationary Operational Environmental Satellite (*17–20*) GOES-11 in Fig. 3. These comparisons may provide useful tests of models of SEP propagation through the inner heliosphere. In all cases, the dose rate peaks in the RAD data occur at later times than the flux peaks in the GOES data. The 7 to 9 March SEP event had three distinct peaks seen by the RAD on 8 and 9 March. The MSL and Earth were nominally connected on the same Parker spiral line (*21*) at this time, and the MSL was only about 1.2 astronomical units from the Sun, but particles arrived at the MSL nearly a full day later than they were seen near Earth. A possible reason for this delay is that GOES-P7 and the RAD are sensitive to different parts of the initial SEP spectrum, which may behave quite differently over time during an event. In addition, there were at least two events [flares and fast coronal mass ejections (CMEs)] seen in the 7 to 9 March time frame. The first one, on 7 March 0036 UT, was directed at −60° longitude (east of the central meridian as viewed from Earth) and the second on 9 March 0425 UT at 0° longitude (directly at Earth). The differences in arrival times may have been caused by a disturbed Parker spiral from the first CME, so it is possible that the MSL and Earth (GOES) were not actually on or near the same field line during the event.

The SEP fluxes observed by the RAD are dominantly protons, for which $Q(L)$ ($L$, linear energy transfer) is approximately 1. Dose and dose equivalent rates are therefore approximately equal. Table 1 shows the dose equivalent totals recorded during the three periods of measurable solar activity. SEP doses were obtained by subtracting average GCR dose rates from the total for the days shown. The SEP total from these five events is roughly equal to 15 days of GCR dose equivalent during low solar activity.

The MSL's cruise to Mars took 253 days. Treating the measured GCR dose equivalent rate of 1.84 mSv/day as constant during the entire cruise, the estimated total dose equivalent from both GCR and SEP events is 466 ± 84 mSv, with about 5.4% attributable to SEPs. This result is a strong function both of the time in the solar cycle during which the cruise occurred and of the shielding surrounding the RAD during the cruise. The crew exposures during a human mission to (and returning from) Mars would no doubt differ from our findings because of these effects. Actual exposures will of course depend on the details of the habitat shielding and the unpredictable nature of large SEP events. Even so, our results are representative of a trip to Mars under conditions of low to moderate solar activity.

Comparisons between the measured and calculated dose and dose equivalent rates are not sufficient to fully validate or benchmark transport models, but they are highly relevant here because astronaut exposure calculations are made with transport models. It is therefore essential that such models be as accurate as possible, and accuracy is obtained through an iterative process of model development and comparisons with data. Agreement with measured dose or dose equivalent rates is a necessary part of model validation. Although there has been considerable previous work in this area, including recent articles by Schwadron *et al.* (*22*) and McKenna-Lawlor *et al.* (*23*), for present purposes we restrict the discussion to the models used most recently by the NASA Johnson Space Center (JSC), which is responsible for assessing crew exposures (*24*, *25*). The tools used by JSC include the Badhwar-O'Neill GCR model (*26*, *27*), the HZETRN transport model (*28–30*), and pion transport codes (*31–33*). See the supplementary materials for details.

Four transport calculations are shown in Table 2, corresponding to permutations of the JSC model (two versions of the GCR flux model, with pion production simulated or not). These are point values at the RAD position. In all cases, dose and dose equivalent were calculated at several depths of shielding, and polynomials were fit piecewise. The polynomials were integrated against the shielding distribution to obtain the results shown here. It is clear that pions and their decay products make an important difference in the calculated dose under shielding, whereas their contribution to dose equivalent is relatively small, owing to the low LET of the particles. The RAD cruise measurements are shown in the last row of Table 2. For dose rate, the Badhwar-O'Neill 1996 (BO-96) results with and without pions bracket the central value of the measurement, both falling within the range of experimental uncertainty. The dose rate predicted by BO-11 with pions included is close to the central value of the data, whereas BO-11 without pions gives a result outside the $1\sigma$ error bar. Predicted dose equivalent rates are comparatively insensitive to these model variations, and all are slightly smaller than the measurement but within the $1\sigma$ error on the data. The calculated $\langle Q \rangle$ values are more sensitive to variations in the model than are the dose equivalent rates, and only the BO-96 model without pions and the BO-11 model with pions give values that are within the $1\sigma$ experimental uncertainty.

Some of the dose and dose equivalent from GCRs during the cruise is attributable to neutral particles (neutrons and $\gamma$ rays). A full analysis of these contributions requires the application of an inversion technique (*34*), but a simplified first-order estimate shows that the measured neutral particle contribution was less than 10% of the total.

**Table 2. Measured and calculated GCR dose and dose equivalent rates.**

| GCR flux model | Pions/included in transport | Dose rate (µGy/day) | Dose equivalent rate (mSv/day) | <*Q*> |
|---|---|---|---|---|
| Badhwar-O'Neill 1996 | No | 0.429 | 1.69 | 3.95 |
| | Yes | 0.507 | 1.70 | 3.53 |
| Badhwar-O'Neill 2011 | No | 0.366 | 1.72 | 4.69 |
| | Yes | 0.445 | 1.80 | 4.05 |
| RAD measurement | | 0.481 ± 0.080 | 1.84 ± 0.33 | 3.82 ± 0.25 |

Several space agencies (the Russian Space Agency, European Space Agency, and Canadian Space Agency) have adopted the conventional risk assessment approach outlined above, using 1 Sv as the astronaut career exposure limit. Because of the large biological uncertainties for HZE particles, NASA has proposed a different approach, defining *Q*'s in terms of Z and E, and estimates an uncertainty distribution for the *Q* for different particle types (*24*). This approach defines astronaut career limits that correspond to a 3% risk of exposure-induced death for cancer and protects against uncertainties in models using the upper 95% confidence interval. Central estimates of dose limits for 30- to 60-year-old never-smokers range from 600 to 1000 mSv and 800 to 1200 mSv for females and males, respectively (*35*). Dose limits at the 95% confidence levels are about one-third the central values.

NASA's "Design Reference" Mars mission (*36*) posits various cruise durations, with a typical figure of about 180 days. The MSL's cruise was longer than this, but with a human crew aboard, it is likely that faster transits would be selected. Assuming a 180-day one-way duration, similar shielding, and a similar time in the solar cycle, we would expect a crew to receive 331 ± 54 mSv from GCRs, with additional (variable) contributions from SEP events. The return trip would double this, to 662 ± 108 mSv in total. It is clear that the exposure from the cruise phases alone is a large fraction of (and in some cases greater than) currently accepted astronaut career limits. Time spent on the surface of Mars might add considerably to the total dose equivalent, depending on shielding conditions and the duration of the stay. This is problematic for both central estimates of cancer risks and NASA's uncertainty analysis, which imposes a safety factor until confidence intervals are significantly narrowed. In this context, the data provided by the RAD experiment contribute to the reduction of uncertainties by facilitating the improvement of transport models.

The models used by NASA predict that the GCR dose rate is a very weak function of shielding depth (up to 100 g/cm$^2$ of aluminum) because of the high energies of the ions and the copious production of secondary particles. The dose equivalent shows more sensitivity to shielding depth, due to the increasing fraction of heavy ions that fragment as depth increases. Given that the shielding provided by the MSL spacecraft is probably not drastically different from that of the Crew Exploration Vehicle (CEV) or other future vehicles, at least in an average sense, and the modest attenuation of GCR dose with increasing shielding depths, the GCR dose and dose equivalent rates reported here are probably realistic for the expected exposures during future human deep space missions of similar duration. Although only 5% of the contribution to the measured dose equivalent during the MSL's cruise to Mars was from SEP events, it should be remembered that the frequency and intensity of such events are highly variable and that the current cycle appears to be producing a very weak solar maximum (*37*). The SEP contribution could conceivably be many times larger in a different time frame.

### References and Notes

1. *Radiation Hazards to Crews on Interplanetary Missions* (National Academy Press, Washington, DC, 1996).
2. F. A. Cucinotta, M. Durante, *Lancet Oncol.* **7**, 431 (2006).
3. *Quantities and Units in Radiation Protection Dosimetry* (ICRU Report 51, International Commission on Radiation Units and Measurements, Bethesda, MD, 1993).
4. *Recommendations of Dose Limits for Low Earth Orbit* (NCRP Report No. 132, National Council on Radiation Protection and Measurements, Bethesda, MD, 2000).
5. *Information Needed to Make Radiation Protection Recommendations for Space Missions Beyond Low-Earth Orbit* (NCRP Report No. 153, National Council on Radiation Protection and Measurements, Bethesda, MD, 2006).
6. International Commission on Radiological Protection, *Ann. ICRP* **21**, 1 (1991).
7. *Health Risks From Exposure to Low Levels of Ionizing Radiation, BEIR VII Phase 2* (National Academies Press, Washington, DC, 2006).
8. The full spacecraft model contains thousands of components, hence the need for simplification. At present, only a subset of materials within the charged particle telescope's field of view is included in the shielding model, the current state of which is described in the supplementary materials.
9. S. L. Koontz, P. A. Boeder, C. Pankop, B. Reddell, "The ionizing radiation environment on the International Space Station: Performance vs. expectations for avionics and materials," in *Radiation Effects Data Workshop, 2005* (IEEE, 2005), pp. 110–116.
10. J. W. Wilson *et al.*, *Galactic and Solar Cosmic Ray Shielding in Deep Space* (NASA Technical Paper No. 3682, NASA, Hampton, VA, 1997).
11. D. M. Hassler *et al.*, *Space Sci. Rev.* **170**, 503 (2012).
12. A. Posner *et al.*, *Adv. Space Res.* **36**, 1426 (2005).
13. Dose rates as measured by the RAD include particles originating from the MSL's power supply, a radioisotope thermoelectric generator that emits a steady background of neutrons and γ rays. These contributions were measured during ground tests and were subtracted from the results presented here. More details about the background subtraction are given in the supplementary materials.
14. Before 27 January 2012, the RAD observed with a 465-s cadence and nearly 100% duty cycle. Subsequently, RAD observations were 929 s in duration, with a 50% duty cycle, reducing the data volume by a factor of 4 to accommodate steadily decreasing telemetry bandwidth. At the same time as the observing cadence was changed, the sensitivity of the plastic scintillator was increased, resulting in a slightly higher value of the GCR dose rate measured by that detector (~10%, visible in Fig. 1).
15. Simulations indicate that the average value of the ratio *dE/dx* in silicon and LET in water is 1.6 for GCRs, with an associated uncertainty of ±15%. Proper calculation of the range of this ratio must account for the effects of straggling, which is a significant factor in thin silicon detectors such as those in the RAD. The LET conversion factor in turn yields a dose conversion factor of 1.45.
16. The spacecraft shielding was equal for both detectors, but the plastic scintillator is additionally shielded by 1.2 cm of plastic scintillator below and on the sides and 2.8 cm of cesium iodide on top. Proton energies required to penetrate these materials are about 35 and 95 MeV, respectively, as compared to about 10 MeV required for a particle in the telescope field of view to reach the silicon detector used for dosimetry.
17. T. Onsager *et al.*, "Operational uses of the GOES energetic particle detectors," in *Proceedings of SPIE 2812, GOES-8 and Beyond* (SPIE, Bellingham, WA 1996), p. 281.
18. The P7 channel measures the proton flux between 165 and 500 MeV. It was chosen for comparison because the reported ratio of peak flux to quiet-time flux was similar to the ratio of peak dose rate to quiet-time dose rate seen in the RAD in the 27 January event. This comparison is not intended to suggest that the P7 channel and the RAD (under shielding) had similar sensitivities in terms of their energy thresholds or ranges.
19. The use of the quiet-time flux of GOES differential proton flux channels is problematic, especially for the higher-energy channels. The differential fluxes are obtained by subtracting fluxes measured in the various integral channels. As there are by definition no negative fluxes, the algorithm used to obtain differential fluxes assumes a background level that cannot be crossed, as discussed in (*20*). Despite this caveat, the dearth of higher-energy proton data from other spacecraft sources led us to arbitrarily scale the GOES data for comparison to the RAD data.
20. A. Posner, *Space Weather* **5**, S05001 (2007).
21. E. N. Parker, *Astrophys. J.* **128**, 664 (1958).
22. N. Schwadron *et al.*, *Space Weather* **8**, S00E04 (2010).
23. S. McKenna-Lawlor, P. Gonçalves, A. Keating, G. Reitz, D. Matthiä, *Planet. Space Sci.* **63-64**, 123 (2012).
24. F. A. Cucinotta, L. Chappell, M. Y. Kim, *Space Radiation Cancer Risk Projections and Uncertainties–2010* [NASA Technical Paper 2011-216155, NASA Scientific and Technical Information (STI) Program, Hampton, VA, 2011].
25. F. A. Cucinotta, L. Chappell, M. Y. Kim, *Space Radiation Cancer Risk Projections and Uncertainties–2012* (NASA Technical Paper 2013-217375, NASA STI Program, Hampton, VA, 2013).
26. G. D. Badhwar, P. M. O'Neill, *Nucl. Tracks Radiat. Meas.* **20**, 403 (1992).
27. P. M. O'Neill, *IEEE Trans. Nucl. Sci.* **57**, 3148 (2010).
28. J. W. Wilson *et al.*, *HZETRN: Description of a Free-Space Ion and Nucleon Transport and Shielding Computer Program* (NASA Technical Paper 3495, NASA STI Program, Hampton, VA, 1995).
29. F. A. Cucinotta *et al.*, *Radiat. Meas.* **41**, 1235 (2006).
30. T. Slaba, S. R. Blattnig, F. F. Badavi, *J. Comput. Phys.* **229**, 9397 (2010).
31. T. Sato, A. Endo, L. Sihver, K. Niita, *Radiat. Environ. Biophys.* **50**, 115 (2011).
32. S. K. Aghara, S. R. Blattnig, J. W. Norbury, R. C. Singleterry, *Nucl. Instrum. Methods* **B264**, 1115 (2009).
33. R. B. Norman, S. R. Blattnig, G. De Angelis, F. F. Badavi, J. W. Norbury, *Adv. Space Res.* **50**, 146 (2012).
34. J. Köhler *et al.*, *Nucl. Instrum. Methods* **B269**, 2641 (2011).
35. F. A. Cucinotta, L. J. Chappell, *Radiat. Res.* **176**, 102 (2011).
36. B. G. Drake, S. J. Hoffman, D. W. Beatty, "Human exploration of Mars, Design Reference Architecture 5.0," in *Aerospace Conference, 2010 IEEE* (IEEE, 2010), pp. 1–24.

37. For 2012, the average modulation potential derived from the Earth-based Oulu neutron monitor (*38*) was less than 700 MV, as compared to values of 1000 MV or greater seen in previous solar maximum periods. The full range of the modulation potential (Φ) during the cruise as measured by the Oulu neutron monitor is available at http://cosmicrays.oulu.fi/phi/Phi_mon.txt.
38. I. G. Usoskin, K. Alanko-Huotari, G. A. Kovaltsov, K. Mursula, *J. Geophys. Res.* **110**, A12108 (2005).
39. A. I. Mrigakshi, D. Matthiä, T. Berger, G. Reitz, R. F. Wimmer-Schweingruber, *J. Geophys. Res.* **117**, A08109 (2012).

**Acknowledgments:** The RAD is supported by NASA (Human Exploration and Operations Mission Directorate) under Jet Propulsion Laboratory (JPL) subcontract 1273039 to the Southwest Research Institute and in Germany by the German Aerospace Center (DLR) and DLR's Space Administration, grant numbers 50QM0501 and 50 QM1201, to the Christian Albrechts University, Kiel. Part of this research was carried out at JPL, California Institute of Technology, under a contact with NASA. We appreciate discussions with P. O'Neill and M. Kim at NASA's JSC and with S. Blattnig, F. Badavi, T. Slaba, and C. Mertens of NASA's Langley Research Center. We extend thanks to J. Simmonds, J. Grotzinger, J. Crisp, A. Vasvada, H. Mortensen, and the Operations Product Generation Subsystem team at NASA-JPL. We also thank M. Meyer, E. Stolper, G. Allen, C. Moore, and V. Friedensen at NASA headquarters and H. Witte at DLR in Germany for their support of the RAD over the years. The data used in this paper are archived in the NASA Planetary Data System's Planetary Plasma Interactions Node at the University of California, Los Angeles. The archival volume includes the full binary raw data files, detailed descriptions of the structures therein, and higher-level data products in human-readable form. The PPI node is hosted at http://ppi.pds.nasa.gov/.

**Supplementary Materials**

www.sciencemag.org/cgi/content/full/340/6136/1080/DC1
Materials and Methods
Supplementary Text
Figs. S1 to S3
References (*40, 41*)

1 February 2013; accepted 12 April 2013
10.1126/science.1235989

---

# An Adaptive Response to Uncertainty Generates Positive and Negative Contrast Effects

**John M. McNamara,[1] Tim W. Fawcett,[2]* Alasdair I. Houston[2]**

**Successive contrast effects, in which behavior is dependent on whether conditions are currently better or worse than they were before, are a striking illustration of the fact that animals evaluate the world in relative terms. Existing explanations for these effects are based on descriptive models of psychological and physiological processes, but little attention has been paid to the factors promoting their evolution. Using a simple and general optimality model, we show that contrast effects can result from an adaptive response to uncertainty in a changing, unpredictable world. A wide range of patterns of environmental change will select for sensitivity to past conditions, generating positive and negative contrast effects. Our analysis reveals the importance of incorporating uncertainty and environmental stochasticity into models of adaptive behavior.**

Humans, like many other animals, make relative judgments about the world. When making decisions, we compare options to other available options (*1–3*) or to situations that we have experienced in the past (*4*). We care about whether we are better or worse off than before, or than we might otherwise be, had things turned out differently (*5, 6*).

A striking illustration of this is successive contrast effects, in which the conditions an individual has experienced in the recent past alter its response to current conditions (*4*). Crespi (*7*) demonstrated successive contrast effects in laboratory rats trained to approach a food reward at the end of a runway apparatus. The rats ran faster toward the reward if they had previously been trained with smaller reward amounts, as compared to control rats that had experienced the current, larger amount throughout the experiment—a positive contrast effect (*8*). Conversely, rats previously trained with an even larger reward showed a slower approach speed than controls when shifted to the same reward amount (*7*)—a negative contrast effect (*8*). Similar effects have been found in bees (*9*), starlings (*10*), and a variety of mammals (*11–14*), including humans.

Successive contrast effects pose a serious challenge to accounts of rational choice in which past states or alternative current states are irrelevant (*6*). So far, all theories to explain the existence of contrast effects have been based on descriptive models of psychological or physiological processes (*4, 7, 15–18*), largely ignoring their evolutionary basis [though see (*10*)]. Here we address this gap, by developing a simple and general optimality model to show that both positive and negative successive contrast effects can arise from an adaptive response to uncertainty about how conditions change over time.

We consider the behavior of an animal that has to perform work to gain rewards. If the animal expends effort $u$ it gains rewards at rate $\gamma u$, where $\gamma$ represents the profitability of the reward source. To reflect the physiological costs of work (*19*) or risks of exposure to predators (*20*), we assume that the animal's mortality rate, $M(u)$, is an increasing, accelerating function of effort. This imposes a trade-off, for which there is some unique level of effort that maximizes the animal's expected lifetime reward (*21*).

In the scenario we consider, the profitability of the reward source fluctuates stochastically over time. The animal can perceive its current profitability $\gamma$ but does not know when this will change. While still alive, we assume that it pays some small maintenance costs ($b$ energy units per unit of time) and invests all remaining gains directly into reproduction, so its rate of reproductive success is $\gamma u - b$. Under these conditions, to maximize its fitness (expected lifetime reproductive output), the animal must maximize $\gamma u - M(u)V$, where $u$ is its current effort and $V$ its expected future reproductive success (*22*). Broadly, we can interpret $\gamma$ as the value of work and $V$ as the value of the animal's life (*21*). Differentiating this expression with respect to $u$, we see that the optimal effort, $u^*$, that maximizes fitness will satisfy $M'(u^*) = \gamma/V$. Because $M$ is an increasing,

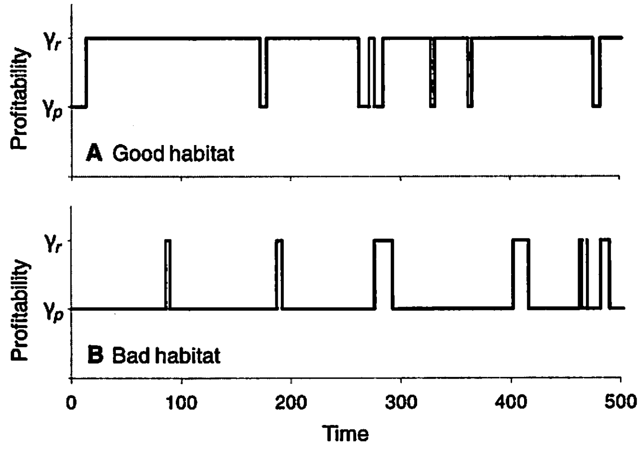

**Fig. 1. Examples of the stochastic fluctuations in the profitability of a reward source over time in a (A) good or (B) bad habitat.** The animal can perceive whether the source is currently rich (profitability $\gamma_r$) or poor ($\gamma_p$) but does not know when the next switch will occur, nor which habitat it is in. Parameters: $t_{Gr} = 100$, $t_{Gp} = 10$, $t_{Br} = 10$, $t_{Bp} = 100$.

---

[1] School of Mathematics, University of Bristol, University Walk, Bristol BS8 1TW, UK. [2] School of Biological Sciences, University of Bristol, Woodland Road, Bristol BS8 1UG, UK.

*Corresponding author. E-mail: tim.fawcett@cantab.net